JOM, Vol. 76, No. 9, 2024
https://doi.org/10.1007/s11837-024-06582-7
© 2024 The Minerals, Metals & Materials Society

Microstructural Analysis of Diffusion-Bonded AZ31 Mg Alloy Fabricated by Wire-Arc-Directed Energy Deposition for Lightweight Complex Structures

R. DIPIN KUMAR,[1] YASHWANT KOLI,[1] and S. ARAVINDAN[1,2]

1.—Department of Mechanical Engineering, IIT Delhi, New Delhi 110016, India. 2.—e-mail: aravindan@mech.iitd.ac.in

Additive manufacturing is gaining wide acceptance in the manufacturing industries, but the joining of additively manufactured components is a rarely researched area. In this study, diffusion bonding of directed energy-deposited (DED) Mg alloy (AZ31), using an electric arc as an energy source was analyzed. Diffusion bonding (DB) was performed in a non-vacuum condition with gallium treatment at the faying surfaces to eliminate the oxide formation and promote metallurgical contact. Microstructural and elemental distribution analyses of additively manufactured AZ31 alloy and diffusion-bonded joints were carried out using FESEM and EPMA. EBSD analysis indicated that the bonding interface is characterized by discontinuous dynamic recrystallized grains featured by grain boundary bulging and grain boundary migration. The 90° triple junction observed at the interface migrates to reduce the grain boundary energy. The fine precipitates of β-$Mg_{17}Al_{12}$ were distributed uniformly throughout the material, which enhanced precipitation hardening. High integrity joints without any voids could be obtained by diffusion bonding and the joint line was not discernible. The high-intensity elemental content at the joint interface highlights the enhanced interdiffusion of constituent atoms across the faying surfaces.

INTRODUCTION

Directed energy deposition (DED) is a category of additive manufacturing (AM) processes that involve melting feedstock material in the form of wire or powder by using a focused energy source, such as an arc, laser, or electron beam.[1] The molten pool of feedstock is directed to the build surface layer by layer, as per the 3D model of the component to be built. Near-net-shape products can be obtained upon solidification. DED using an arc (DED-Arc) is a cost-effective AM process to manufacture intricate metallic components. Moreover, DED can be used to repair already existing components, as localized addition of materials is possible. DED-Arc can be achieved by different heat sources, such as a gas metal arc,[2] gas tungsten arc,[3] plasma arc,[4] and cold metal transfer arc.[5] In order to fabricate a component with minimum defects, such as distortion, residual stresses, anisotropy, porosities, etc., a low heat input arc is employed which is one of the desirable characteristics of the cold metal transfer (CMT) process.

Joining of AM components is required owing to the limitation in bed size, repair of components, manufacture of intricate shapes, etc. It is significant to join/repair AM components without inducing fusion defects such as the heat-affected zone (HAZ), porosity, cracking, warpage, etc. In recent years, research has been conducted on the method for joining AM components fabricated by selective laser melting (SLM). Prashanth et al.[6,7] investigated the joining of AM components by friction welding. Enhanced ductility at the expense of reduced strength was reported for friction-welded AM components. Solid-state bonding of Ti6Al4V components fabricated by SLM has been investigated,[8] and dynamic recrystallization (DRX) and

(Received January 20, 2024; accepted April 2, 2024; published online May 3, 2024)

increased microhardness were observed at the joint interface. Nevertheless, the research on joining of DED components is fairly new and lacks prior art. Recently, the joining of an Al-Si alloy manufactured by DED-Arc was investigated.[9] Successful joints were achieved without any formation of intermetallic compounds (IMCs).

The need for lightweight structures in the automobile, aviation, and other similar industries for fuel saving and reduced emissions has resulted in the increasing use of Mg alloys as structural materials.[10] The restricted number of slip systems with the hcp crystal structure reduces the plasticity of magnesium alloys.[11] Therefore, it is difficult to produce complex shapes through conventional metal deformation processes. AZ series Mg alloys are commonly used in automobile industries for the manufacturing of transfer cases, gearbox housings, manual and continuously variable transmission cases, wheels, airbag housings, etc., due to its high specific strength, low density, vibration damping capacity, and good castability.[12] DED-Arc AM of Mg alloys is a highly efficient deposition process compared to powder bed fusion (PBF) AM techniques.[13] PBF techniques require high-power lasers for efficient deposition, which will increase the complexity as the boiling point of Mg is low. Mg alloys have a high probability to evaporate during laser processing, and their high chemical affinity-induced oxidative tendency is prone to affect the binding efficiency.[14] The DED-Arc technique is often referred to as the wire-arc additive manufacturing (WAAM) method.[5,15–17] DED-Arc using CMT as a power source is employed for fabricating large intricate shapes with higher metal deposition rate and low heat input characteristics. However, softer materials like Al alloys and Mg alloys are susceptible to humping defects during WAAM-CMT. Humping is an aesthetic flaw that not only affects the weld bead's appearance but also the mechanical properties because of its uneven profile. It can be reduced by choosing the optimal process parameters in WAAM-CMT.[18] Joining of AM Mg alloys is required for manufacturing lightweight complex structures in automobile industries and for the repair of components.

Diffusion bonding (DB) enables the joining of similar/dissimilar metals and metal matrix composites at elevated temperature and applied pressure without melting the parent material. It enables the joining of precision components having complex internal features, and is classified as a green and sustainable process.[19] The literature has also reported the joining of immiscible materials like tungsten and copper,[20] and materials having large differences in CTE, like W and steel,[21] by diffusion bonding. According to the Arrhenius relationship, the diffusivity increases exponentially with temperature, and hence the atoms disperse across the faying surfaces. It is possible to achieve a homogeneous joint microstructure that resembles the parent metal as a result of the void closure and grain boundary (GB) growth across the contact.

A limited literature has reported on the joining of similar Mg alloys by diffusion bonding. The fine grains evolved due to the superplastic deformation enhanced the GB diffusion and hence facilitated low-temperature bonding of the AZ31 Mg alloy.[22] DB of the AZ91 Mg alloy with an Ag interlayer was analyzed in a vacuum furnace at 480°C. Sound joints were achieved due to the formation of the liquid phase and further solidification at the interface.[23] The as-cast Mg-Gd alloy was diffusion-bonded and a highly efficient joint was obtained at 550°C. The diffusion of the Gd atoms towards the interface and the resulting formation of the precipitated compounds of Mg-Gd enhanced the strength of the joint.[24] Nevertheless, dissimilar joining of Mg alloys and Al alloys through DB has been widely studied without an interlayer,[25,26] with an Ag-Cu-Zn alloy interlayer,[27] with a PVD Ag interlayer,[28] and with a Cu interlayer.[29] However, the literature on diffusion bonding of AM Mg alloys is scarce.

In this article, DED of the AZ31 Mg alloy using the CMT process is utilized to fabricate a single-wall structure. Solid-state diffusion bonding (SSDB) of direct energy-deposited AZ31 Mg alloy using an electric arc (DED-Arc/AZ31) is the novel work. An interface treatment using liquid gallium (Ga) has been carried out to facilitate the bonding in a muffle furnace without a vacuum. DB in non-vacuum conditions considerably reduces the equipment setup cost. SSDB can be considered as a sheet lamination AM process in which metallic sheets can be bonded together to form a monolithic stack.

EXPERIMENTAL

Machine Setup for DED-Arc

Figure 1a shows the manual CMT machine setup (TPS400i; Fronius). The welding torch of the existing CMT machine was coupled with to a flex-track system generally used for pipe joining, as shown in Fig. 1b. This flex-track system has an FRC-45 Pro Controller which controls all the process parameters, such as welding or travel speed, wire feed rate, flow of shielding gas, arc length correction factor, pulse dynamic correction factor, etc., as shown in Fig. 1c. From arc initiation to arc extinguishing, and movement of the torch in all three directions, is regulated by this controller.

Materials and Methodology

AZ31 Mg alloy filler wire of 1.2 mm diameter was used for fabricating the AM single thin-wall structure. The component was fabricated on the AZ31 substrate plate having the same chemical composition as that of the filler wire. The quantitative

electron probe micro-analysis (EPMA; EPMA-1720; SHIMADZU) results of the filler wire justify its chemical composition, which is displayed in Table I.

A DED first layer and subsequently deposited layers on the substrate AZ31 using the CMT torch are illustrated in Fig. 2a and b, respectively. The process parameters for the DED-Arc/AZ31 have been chosen based on the extensive trial tests of a bead on a plate. The weld aesthetics, weld geometry, and tolerance level of repeatability decided the best parameters for AM. In this experiment, the chosen process parameters were current 100 A, welding speed 80 cm/min, contact tube to workpiece distance for the first layer 10 mm, hatch distance for every layer 3 mm, and flow of pure argon as shielding gas 20 L/min. For a single thin-wall structure, 8 layers were deposited over the substrate plate (deposition rate = 0.83 kg/h) with a bi-directional path strategy attained with the help of the flex-track controller. In the bi-directional path strategy, the first layer is deposited on the build platform from point (A) to point (B), and a hatch distance of 3 mm is then provided from point (B) without arcing, as displayed in Fig. 2c. The second layer is deposited on the build surface, i.e., the first layer in the opposite direction. Similarly, subsequent layers are deposited with an average layer thickness of 2 mm to form a near-net-shape single thin-wall structure. A cross-sectional specimen was extracted for microstructural analysis from one side of the AM sample, as shown in Fig. 2c. Specimens of dimensions 18 mm× 10 mm × 4.4 mm were extracted from the DED-Arc/AZ31 for DB, as demonstrated in Fig. 2c. The extracted specimens were ground using SiC paper from 320 to 2000 grit size sequentially to form a flat polished surface. The faying surfaces were polished using alumina paste and ultrasonically cleaned in acetone for 20 min to remove the residues. The surfaces were then treated with SiC paper of 4000 grit size containing Ga (99.99% purity), as shown in the inset in Fig. 2c. The top view of the DED-Arc/AZ31 sample is depicted in Fig. 2d.

The assembled samples were loaded into the microprocessor-controlled muffle furnace which was maintained in an inert environment with an Argon gas (99.99% pure) having a flow rate of 5 L/min, and controlled heating was carried out at 10°C/min, as displayed in Fig. 3. The DB was carried out

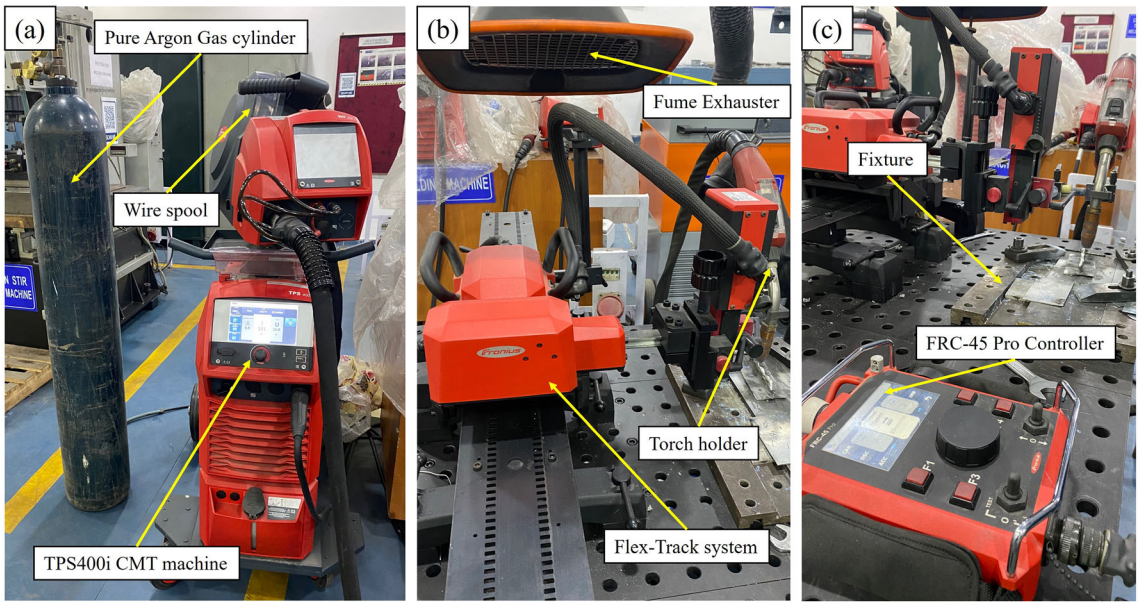

Fig. 1. (a) TPS400i CMT machine setup; (b) flex-track system for torch traveler; (c) FRC-45 Pro Torch controller.

Table I. Quantitative EPMA analysis

No.	Elements	Line	Mass%	Normalized mass%	Mol.%
1	Mg	Ka	62.552	93.946	95.238
2	Al	Ka	3.047	4.576	4.178
3	Si	Ka	0.003	0.004	0.003
4	Mn	Ka	0.227	0.340	0.153
5	Zn	Ka	0.755	1.134	0.427

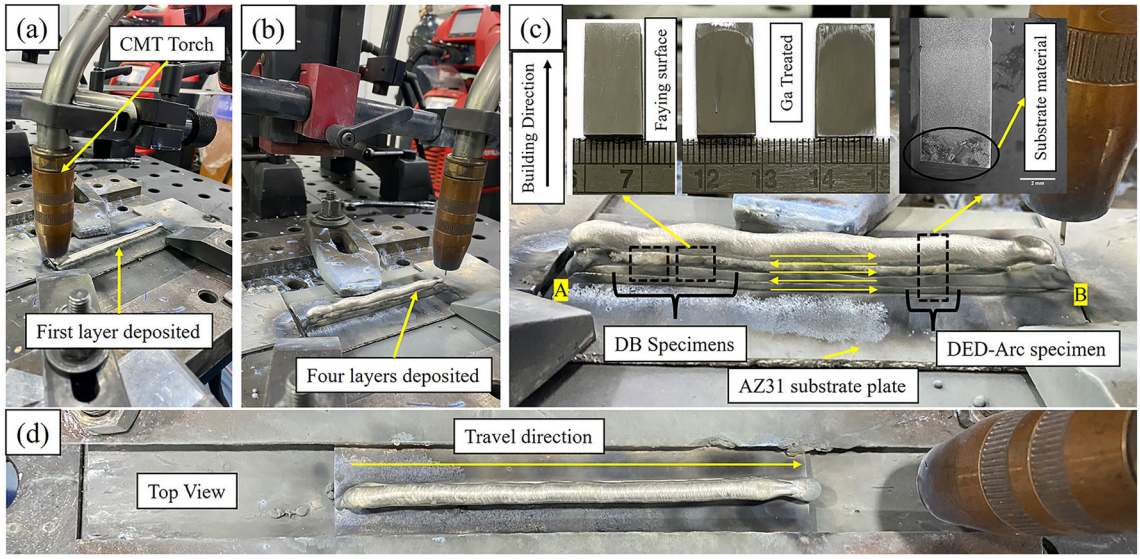

Fig. 2. Fabrication of DED-Arc/AZ31: (a) deposition of the first layer; (b) deposition of subsequent layers with bi-directional path strategy; (c) sample extraction for DB and microstructural analysis; (d) top view of the DED-Arc/AZ31 sample.

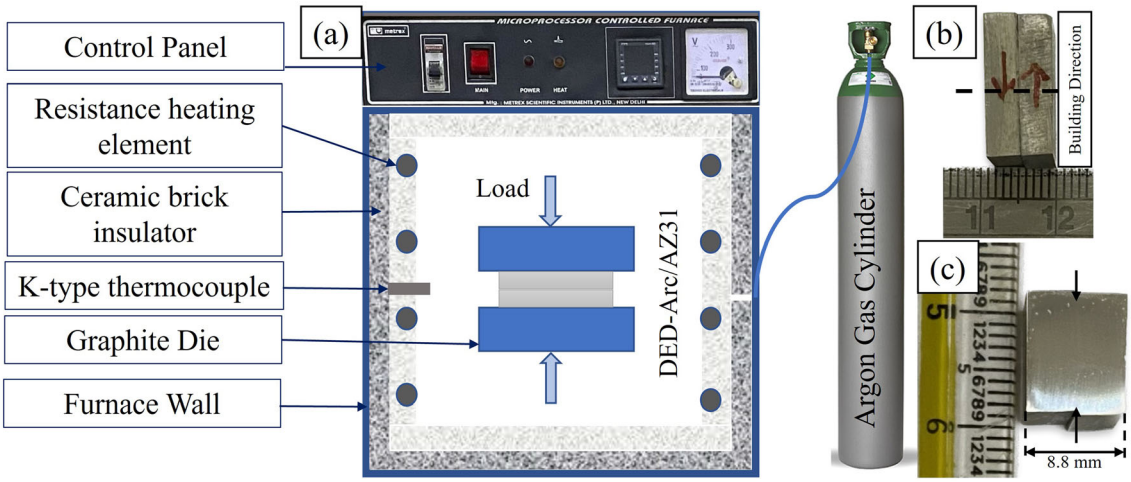

Fig. 3. (a) Equipment setup for diffusion bonding; (b) DB sample showing section plane; (c) polished cross-sectional surface of DB sample.

at the optimized process parameters of temperature 470°C holding time 60 min, and applied pressure 10 MPa, after conducting several trial tests. Three samples were bonded at the reported parameters to ensure reproducibility. The pressure was applied using a mild steel fixture and the fasteners were tightened to achieve the required pressure using a dial torque wrench (CDI, USA). The bonded sample shown in Fig. 3b was allowed to cool to room temperature inside the furnace. The cross-section of the DB sample was extracted using a low-speed abrasive saw machine. Standard metallographic processes were used to grind and mirror-polish the bonded samples, as shown in Fig. 3c, followed by ultrasonic cleaning in acetone and chemical etching using a mixture containing 5 ml acetic acid, 6 g picric acid, 100 ml ethanol, and 10 ml deionized water.

Characterization Techniques

The DED-Arc/AZ31 Mg alloy and DB samples were characterized using an optical microscope (DMLM; LEICA) and field-emission scanning electron microscopy (FESEM; TESCAN MAGNA) with energy dispersive X-ray spectroscopy (EDS). The elemental distribution was analyzed using EPMA. EBSD mapping was carried out at a step size of 0.4 μm with a Nordlys detector (Oxford Instruments) attached to the JEOL JSM-7800F FESEM. HKL Channel 5 software was used for the analysis. To examine the phase formation during DED-Arc, X-ray diffraction (XRD; Ultima IV; Rikagu) analysis was performed on the middle layer with Cu K_α radiation at a scan speed of 3°/min in the 2θ range from 20° to 80°. Grain size analysis by the line intercept method was carried out using ImageJ

software. The microhardness of the DED-Arc and DB samples were analyzed using a Struers Duramin-40 semiautomatic microhardness tester. A 20-g load was applied for 15 s in accordance with ASTM standard E92-17. Microhardness was measured along the building direction of the DED-Arc sample and across the bond line of the DB specimen.

RESULTS AND DISCUSSION

Microstructural Analysis of DED-Arc/AZ31

To investigate the microstructure, a specimen was cut from the AM sample consisting of 8 layers and substrate material, as shown in Fig. 4a. The implementation of the first layer over the substrate

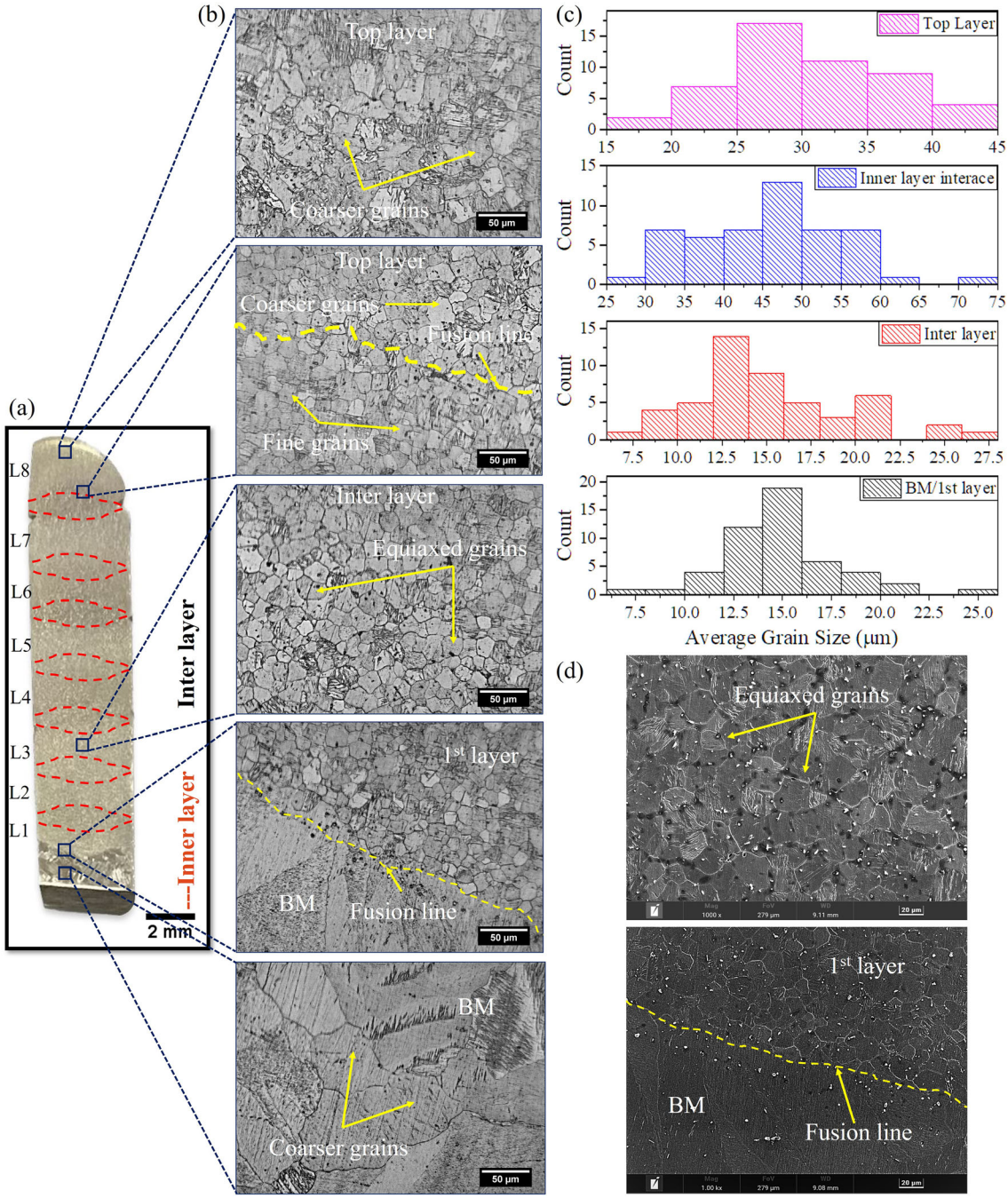

Fig. 4. Average grain size analysis in the inter layer and inner layer: (a) macro-image showing the various inner and inter layer; (b) optical microscopy images for microstructural analysis; (c) average grain size; (d) magnified FESEM images showing the equiaxed grains in the inter layer and the fusion line between the BM and the 1st layer.

material (AZ31) gives a measure of bead geometry. The bead geometry (i.e., weld penetration, weld reinforcement, weld width, contact angle, % dilution) is studied to attain the best process parameters to fabricate the near-net-shape AM sample. Deposition of subsequent layers creates a HAZ which is specified as the inner layer and the actual layers deposited are specified as the inter layers, as displayed in Fig. 4a. The red dotted line shows the inner layer, while the inter layers are specified as L1–L8. The optical microscopy images of the AM specimens are displayed in Fig. 4b. The average grain size of the base metal (BM) and the deposited layers was measured using ImageJ software by the line intercept method, as displayed in Fig. 4c. The average grain size at the interface of the BM and the 1st layer was 15.02 ± 0.2 μm whereas the top layer was 30.36 ± 0.5 μm. This is due to the softening behavior caused by the heat accumulation effect (HAE) along the building direction, i.e., from the first layer to the top layer. The substrate material dissipates heat from the bottom layers due to their close proximity and a higher cooling rate, resulting in finer grains. The heat dissipation rate decreases with distance from the substrate and heat accumulation, due to subsequent depositions resulting in coarser grains. The major effect of this heat accumulation is in the inner layer, where the grains are coarsened compared to the inter layers. Wang et al.[15] reported grain coarsening in the building direction of the AZ31 Mg alloy fabricated by WAAM. The inner layer, which is a HAZ region between the two adjacent layers, revealed the average grain size to be 46.37 ± 0.4 μm whereas the inter layer average grain size was 14.01 ± 0.3 μm. This observation is similar to the general welding conditions where HAZ has coarser grains and fabricated objects have finer grains, as reported by Takagi et al.[13] The maximum average grain size in a single-wall structure is at the inner layer due to the re-melting and re-solidification of the deposited layers. Overall, the single-wall structure is composed of mainly fine equiaxed grains in the inter layers, and comparatively coarser grains in the inner layer. There is no sign of columnar grains which induce anisotropy. The formation of fine equiaxed grains during WAAM of the Mg alloy was reported by Klein et al.[30] and the growth restriction factor was explained using interdependence theory.

The FESEM analysis of the inter layers indicated that the DED-Arc/AZ31 microstructure comprises equiaxed grains with fine precipitates dispersed uniformly along the GBs. The resultant fine-grained structure is due to the rapid cooling during the process of DED-Arc. The dark-colored regions in Fig. 5a represent α-Mg, the light gray colored region represents eutectic α-Mg, and the bright white-colored precipitates are β-$Mg_{17}Al_{12}$. The $Mg_{17}Al_{12}$ phase was precipitated from the super-saturated solid solution of α–Mg due to non-equilibrium cooling during DED-Arc/AZ31. During equilibrium cooling of AZ31, α-Mg and Al_8Mn_5 precipitate first, and Al_8Mn_5 further transforms to $Al_{11}Mn_4$ and Al_4Mn during the subsequent temperature drop.[16] In DED-Arc/AZ31, Al_8Mn_5 is retained in the final microstructure due to the rapid cooling, as evident from the XRD analysis shown in Fig. 5b. The fine precipitates of Al_8Mn_5 formed within the α-Mg matrix are highlighted using the high-magnification FESEM image shown as the inset in Fig. 5a. Hence the non-equilibrium microstructure of DED-Arc/AZ31 consists of primary α-Mg, eutectics (α-Mg and β-$Mg_{17}Al_{12}$), and dispersions of Al_8Mn_5. Moreover, the intensity of the precipitates is higher in the AM sample, indicating more precipitated phases compared to the substrate material. The β-$Mg_{17}Al_{12}$ precipitates hinder the dislocation movement, causing stacking of dislocations near the precipitated phases, and thus increasing the mechanical properties. Moreover, these precipitates pin the GBs, resulting in the formation of fine grains.[31]

Microstructural Analysis of DB Joint Interface

There was no obvious macro-deformation of the specimens due to the DB thermal cyclic process, and the thickness of the DB sample was 8.8 mm, as shown in Fig. 3c. Moreover, the bond line was not discernible with the naked eye so a visually defect-free weld has been achieved. This indicates that the DB process parameters chosen were appropriate. Microstructural analysis of the joint interface, elemental distribution in the diffusion reaction zone, and formation of phases are described in the following sub-sections.

Microstructural analysis of the DB sample was conducted using FESEM equipped with EDS. To reveal the bond line, the DB sample was etched, and the corresponding FESEM micrograph is shown in Fig. 6a. The joint line is free of voids, which indicates that a high-integrity joint has been achieved. The void closure at the interface occurs due to the surface diffusion of atoms and creep-assisted plastic flow of the material. The interface is characterized by fine grains, as highlighted in Fig. 6a, and recrystallization mechanism is explained by EBSD analysis. The eutectic temperature of the Mg-Al alloy is 437°C and the DB thermal annealing was carried out at 470°C. This may result in the redissolution of second-phase particles, and furnace-cooling favors the reprecipitation of β-$Mg_{17}Al_{12}$ as discontinuous particles.[3] Due to furnace-cooling, equilibrium conditions persist during DB and the second-phase particles precipitate from the super-saturated solid solution at around 150°C.[3,16] The bond line is also decorated with the random distribution of second-phase

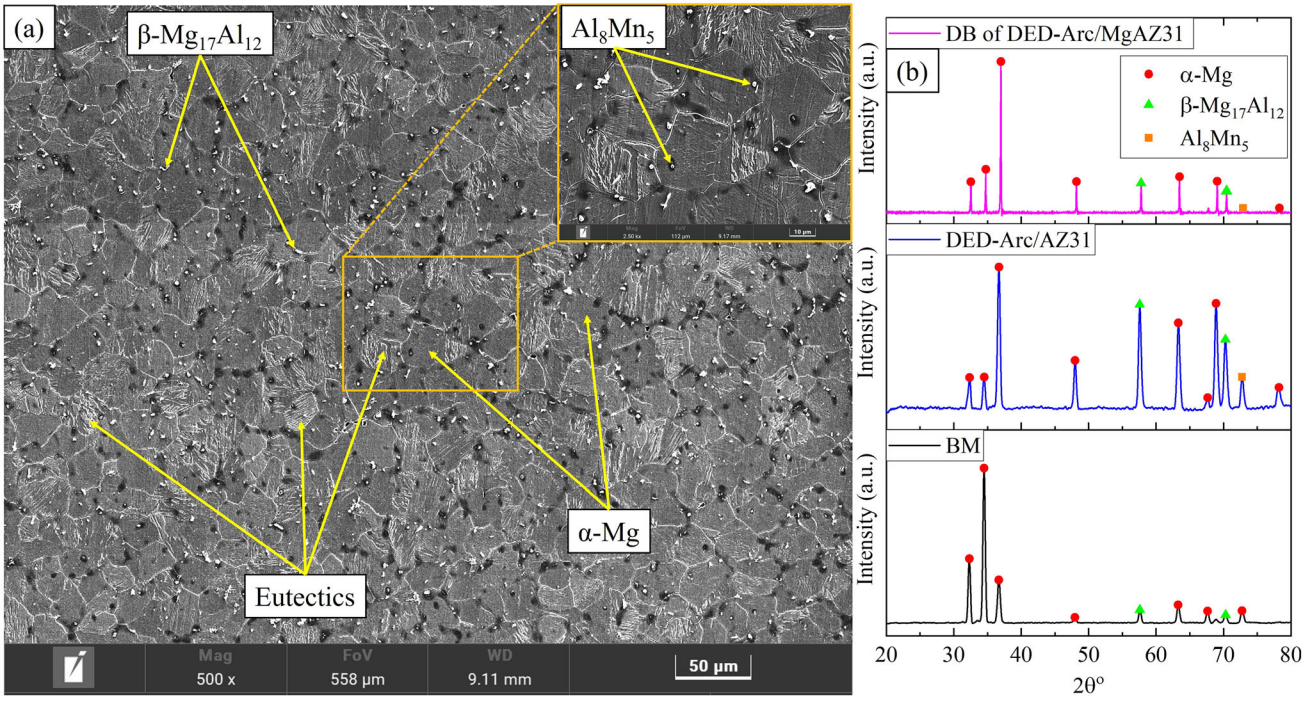

Fig. 5. (a) FESEM image of DED-Arc/AZ31; (b) XRD plots of AZ31 base material and DED-Arc/AZ31.

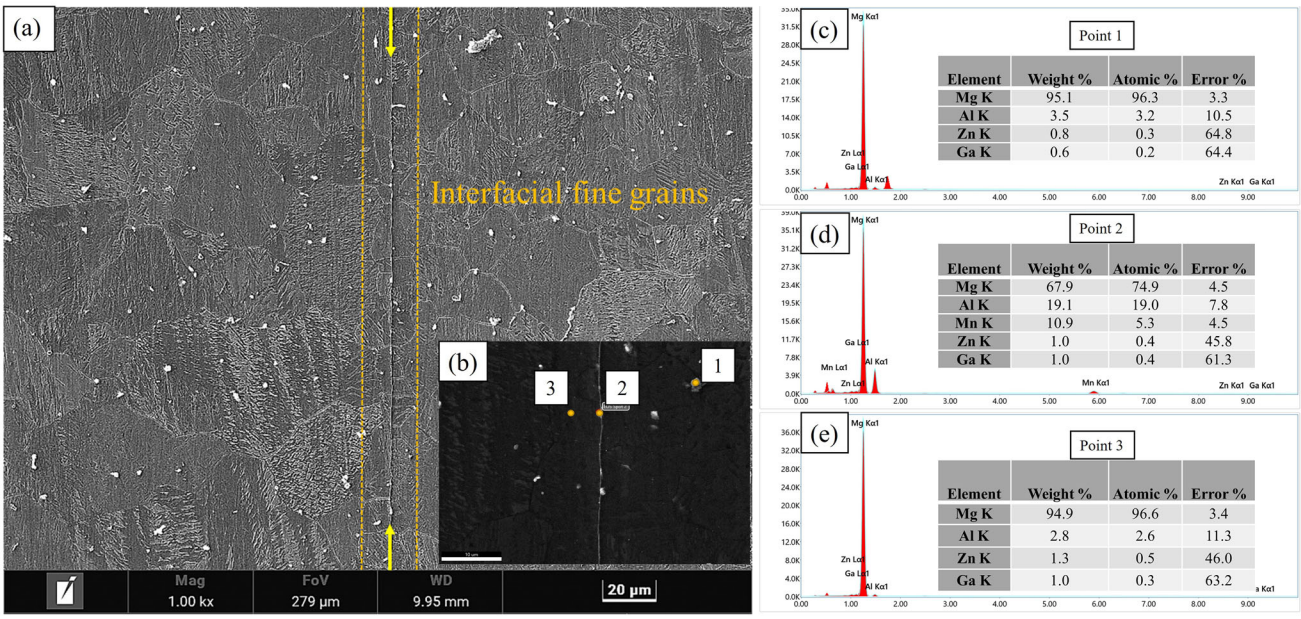

Fig. 6. (a) FESEM image of DB of DED-Arc/MgAZ31; (b) point EDS analysis of DB of DED-Arc/AZ31; (c) point 1; (d) point 2; (e) point 3.

particles, highlighting the diffusion of solute elements in addition to the Mg, which in turn leads to solid-solution strengthening.

EDS point analysis of the DB sample was conducted, as shown in Fig. 6b. The white particle at the interface (point 2) is enriched with Mg and Al elements, as shown in Fig. 6d, which shows that the precipitates are $Mg_{17}Al_{12}$ particles. The atomic percentage (at.%) of Ga at the interface, as shown in Fig. 6d, is 0.4, and it drastically reduced to 0.2 at.% at 15 μm from the interface, as shown in Fig. 6c. This demonstrates that only a trace amount of Ga is retained at the interface post-treatment of the faying surfaces, and that the diffusion of Ga is limited to the diffusion reaction zone.

The EBSD analysis of joint interface is shown in Fig. 7. The inverse pole figure (IPF) map indicates that there is no preferential orientation of grains in the DB region as shown in Fig. 7b. The local average misorientation (LAM) map depicted in Fig. 7d

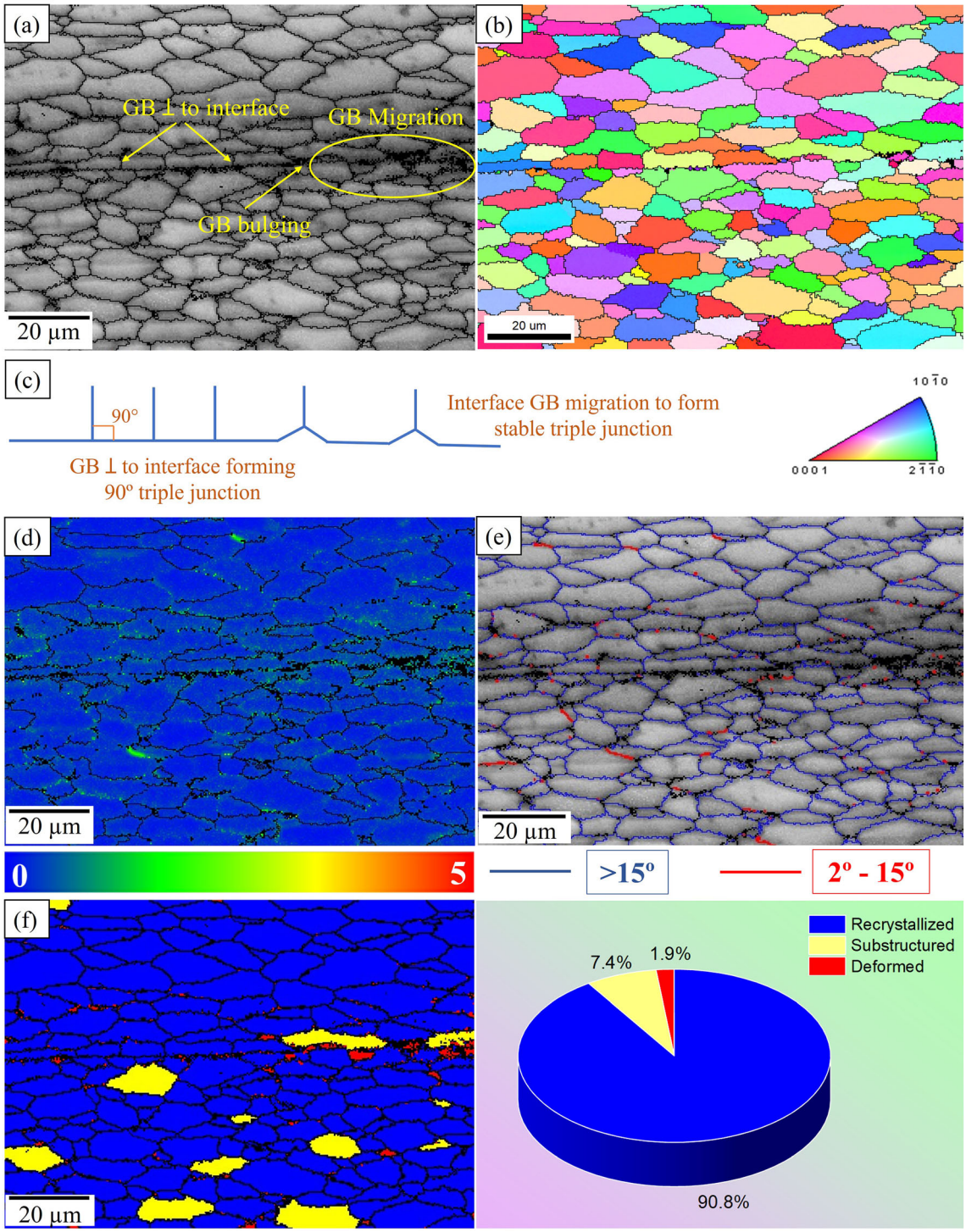

Fig. 7. EBSD analysis of DB joint interface: (a) band contrast map; (b) IPF map; (c) interfacial GB migration; (d) LAM map; (e) GB orientation; (f) recrystallization condition.

indicates the extent of plastic deformation and residual strain in the material. The scale of misorientation is in the range of 0° to 5° and the LAM_{avg} was observed to be less than 3°. The increased strain near the interface indicated by the LAM map was as a result of plastic deformation of asperities during the initial contact under loading. The plastic deformation of the asperities will lead to an increased real contact area and enhances the metallic contact. Moreover, fine grains of 9.24 ± 0.5 μm were observed near the joint interface. The localized plastic deformation due to induced strain and the increased accumulation of dislocations near the interface might have resulted

in DRX in the diffusion reaction zone during the holding time. According to Zhang et al.[32] a fine–fine grain interface has been observed when complete recrystallization has occurred on either side of the bonded region, which in turn leads to a sound joint. The high density of GBs near the interface will in turn result in enhanced diffusion, as the GBs act as the diffusion channels. However, the induced strain will lead to an energy gradient near the interface, which acts as driving force for GB migration. Discontinuous dynamic recrystallization (DDRX) featured by GB bulging and strain-induced GB migration was observed, as highlighted in the band contrast map (Fig. 7a).

GBs of the base metal perpendicular to the interfacial GB were observed at the interface, indicating the formation of 90° triple junctions (TJs). Such TJs have high surface tension and hence try to reduce the GB energy by migrating across the interface,[32] as depicted in Fig. 7c. The most stable GB TJs form an angle of 120° according to the force equilibrium conditions. Hence, some GBs gradually migrate across the interface to reduce the energy and form a wavy interface. With finer grains at the interface, high numbers of GBs intersect the original interface and more interfacial GB migration occurs at the TJs, which will lead to good bonding.

Figure 7e shows the band contrast map superimposed with GB angle orientation where high-angle grain boundaries (HAGBs) (> 15°) are indicated by blue lines, and low-angle grain boundaries (LAGBs) (2–15°) are indicated by red lines. Figure 7f shows the recrystallized, sub-structured, and deformed condition of grains in the DB region. Of the grains, 90.8% are recrystallized with mainly HAGBs at the interface, indicating that DDRX has occurred.[33] DDRX is characterized by nucleation of grains at the HAGBs and growth by long-range migration. The observation of GB bulging in the interface region indicates that DDRX has resulted in the formation of new finer grains.[34] During the holding time, the softening of interface grains leads to the deformation of some grains at the interface, as shown in Fig. 7f. Thus, the process of DB of DED-Arc/AZ31 consists of plastic deformation at the interface, DDRX, and strain-induced GB migration.

Elemental Distribution Analysis Using EPMA of DB Joint Interface

The macrograph of the DB sample of DED-Arc/AZ31 is shown in Fig. 8a appearing as a monolithic block. The black arrows show the bond line. The FESEM image of the bonded region is displayed in Fig. 8b for which elemental area mapping has been carried out using EPMA. The distributions of Mg, Al, Ga, Mn, and Zn are displayed in Fig. 8c–g, respectively. The EPMA quantitative analysis of α-Mg (point 1) and eutectic α-Mg (point 2) is also highlighted in Fig. 8. The elemental contents of Al, Mn, and Zn show a slight increasing trend and Mg shows a decreased content in eutectic α-Mg. It is worthwhile to note that the major element Mg is distributed uniformly across the DB region as indicated in Fig. 8c. The white-colored precipitates visible in the FESEM image are either β-$Mg_{17}Al_{12}$ or Al_8Mn_5 particles, as these regions show the comparatively high intensity of Al shown in Fig. 8d.

These particles are formed as the solidifying α-Mg dendrites push the solute elements (Al, Zn, etc.) into the interdendritic liquid and the eventual nucleation of the β-$Mg_{17}Al_{12}$ phase,[35] which is precipitated in the interdendritic region, whereas Al_8Mn_5 appears as dispersions in the α-Mg matrix.[16] It is assumed that the Al_8Mn_5 particles precipitated in the DED-Arc/AZ31 are also retained in the DB sample as the dissolution of the Al-Mn phases may not occur at the bonding temperature. Figure 8e shows that there is no significant accumulation of Ga at the interface, which is desirable. The thin stable oxide film on the faying surface hinders the integrity of the DB joint in the case of the Al and Mg alloys and needs to be prevented.[22] The presence of a trace amount of Ga, which is smeared at the abutting surface by surface treatment, prevents reoxidation at high temperatures, enhances metallic contact, and results in a sound metallurgical joint. Ga surface treatment prior to DB was previously reported for Al alloys[36,37] and dissimilar joining of stainless steel and Ti,[38] and successful bond formation has been reported by alleviating oxide-related problems.

EPMA line analysis across the DB specimen was carried out, as indicated in Fig. 9, from which it can be seen that, in the positions where the normalized intensity of the major alloying element, Mg, is dropping, there is a rise in the intensity of Al and Zn. This is because of the more elemental content of Al and Zn in eutectic α-Mg and β-$Mg_{17}Al_{12}$ than in primary α-Mg. The content of Mg drops as it moves from primary α-Mg to β-$Mg_{17}Al_{12}$. These findings are in line with the EDS analysis and EPMA quantitative analysis discussed in the previous sections. The normalized intensity of Mg at the joint is as high as that of the parent material, as depicted in Fig. 9b. Furthermore, the distribution of other alloying elements such as Zn and Al follows the same trend as that of the base metal. The EPMA qualitative analysis at the joint interface highlights the elemental mass percentages of Mg, Al, and Zn as 96.88%, 2.78%, and 0.34%, respectively, which indicates the enhanced dispersion of atoms across the joint interface at the bonding temperature and pressure. The bell-shaped line distribution of Ga is as expected, and the diffusion distance is limited to a diffusion reaction zone which is also consistent with the EDS analysis.

The diffusion behaviour of atoms is a highly temperature-dependent phenomenon according to the Arrhenius relationship and is explained by the diffusion coefficient.[39] The pre-exponential factor

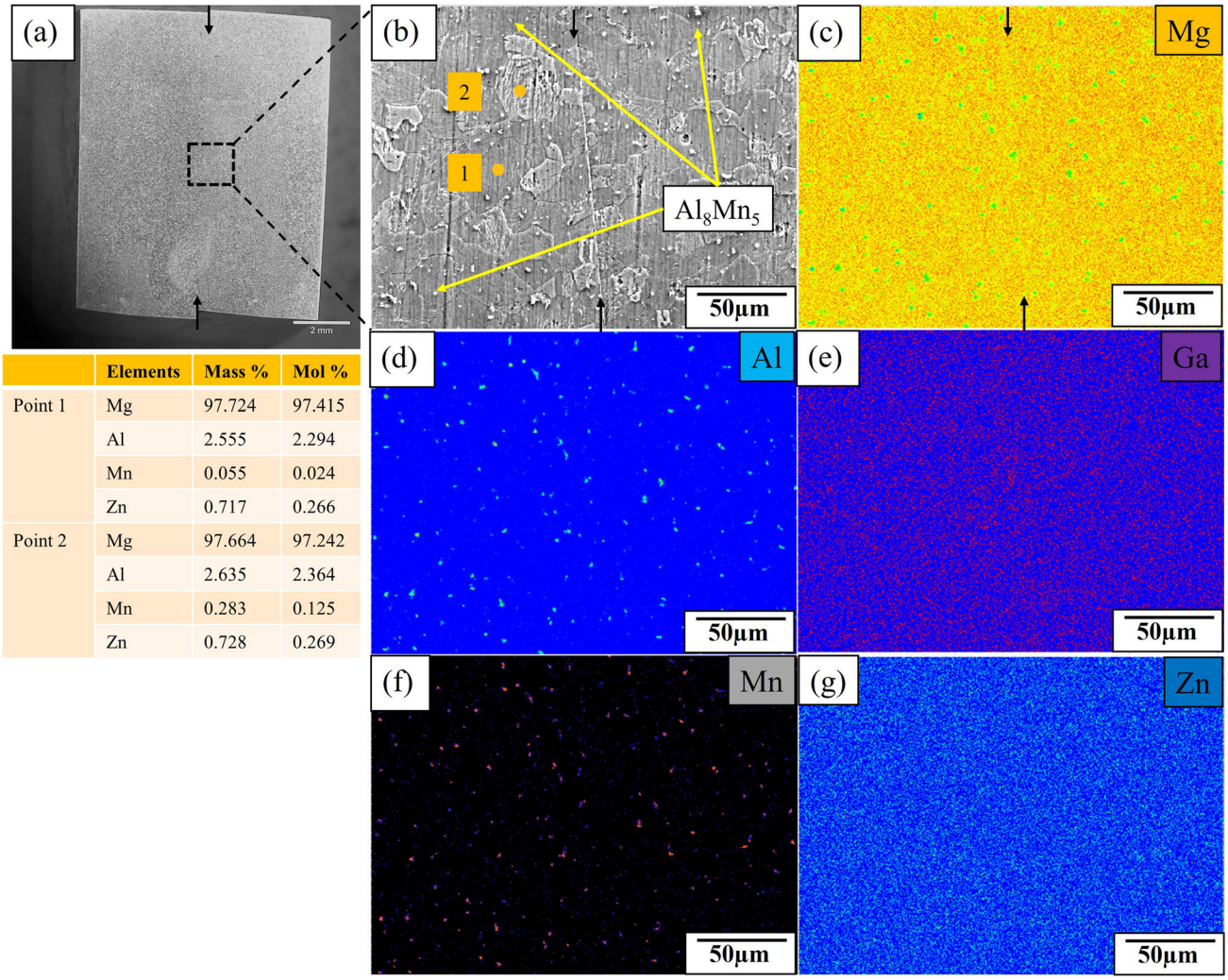

	Elements	Mass %	Mol %
Point 1	Mg	97.724	97.415
	Al	2.555	2.294
	Mn	0.055	0.024
	Zn	0.717	0.266
Point 2	Mg	97.664	97.242
	Al	2.635	2.364
	Mn	0.283	0.125
	Zn	0.728	0.269

Fig. 8. Elemental area mapping using EPMA: (a) macro-image of DB DED-Arc/AZ31; (b) FESEM image; (c) Mg; (d) Al; (e) Ga; (f) Mn; (g) Zn.

(D_o) and activation energy (Q) of Ga in HCP-Mg were experimentally verified as 1.4×10^{-5} m^2/s and 116,869 J/mol, respectively.[40] Hence, the diffusion coefficient of Ga in HCP-Mg at the DB temperature of 743 K was calculated as 8.49×10^{-14} m^2/s. From the simplified solution of Fick's law of diffusion ($x = (Dt)^{1/2}$), the diffusion distance was found to be 17.5 μm. The calculated diffusion length has a good correlation with the observed diffusion length. The small increase in the observed diffusion length of Ga is due to the furnace cooling after the dwell time. From the Ga–Mg system, the eutectic composition will be formed at a temperature of 422.7°C and 19.13 at.% Ga (40.43 mass% Ga) ($L \rightleftharpoons Mg + Mg_5Ga_2$).[41] The maximum mass% of Ga from the EPMA line analysis of the DB sample was 0.31, and the bonding temperature was 470°C. Hence, no eutectic will be formed at the joint interface due to the reaction between Mg and Ga, as the concentration of solute atoms is very much less, but results in the formation of a solid solution of α-Mg. The XRD analysis of the DB DED-Arc/AZ31, as illustrated in Fig. 5b, also shows that no deleterious IMCs are formed between Mg and Ga, which is significant for good quality joints. The Ga-Mg system shows that the maximum solubility of Ga in the terminal solid solution of α-Mg is 3.14 at.%, and that the solubility of Mg in Ga is negligible.

Microhardness Variation of DED-Arc/AZ31 and DB Joints

The microhardness variation observed in the cross-section of DED-Arc/AZ31 along the building direction is depicted in Fig. 10. The variation in microhardness is in line with the variation of grain size in various zones in the DED-Arc/AZ31 specimen. The microhardness difference follows the Hall–Petch relationship, where the inner layer having coarser grains exhibits a smaller microhardness of 53.83 $HV_{0.02}$, as indicated by point L12 (inner layer between layer 1 and layer 2) in Fig. 10, whereas the inter layers, having fine equiaxed grains, show the higher microhardness of 69.92

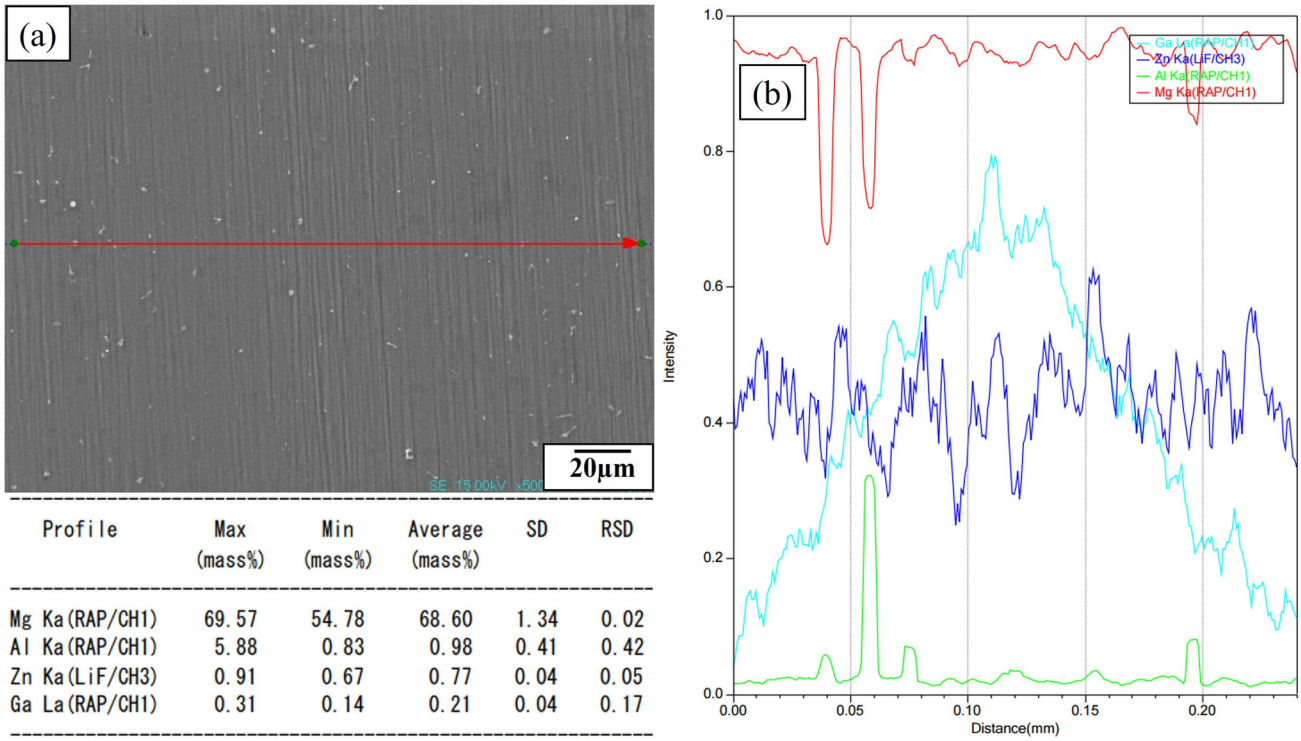

Profile	Max (mass%)	Min (mass%)	Average (mass%)	SD	RSD
Mg Ka(RAP/CH1)	69.57	54.78	68.60	1.34	0.02
Al Ka(RAP/CH1)	5.88	0.83	0.98	0.41	0.42
Zn Ka(LiF/CH3)	0.91	0.67	0.77	0.04	0.05
Ga La(RAP/CH1)	0.31	0.14	0.21	0.04	0.17

Fig. 9. EPMA line analysis: (a) micrograph of DB DED-Arc/MgAZ31 indicating the *line*; (b) distribution of elements across the joint interface and its quantitative analysis.

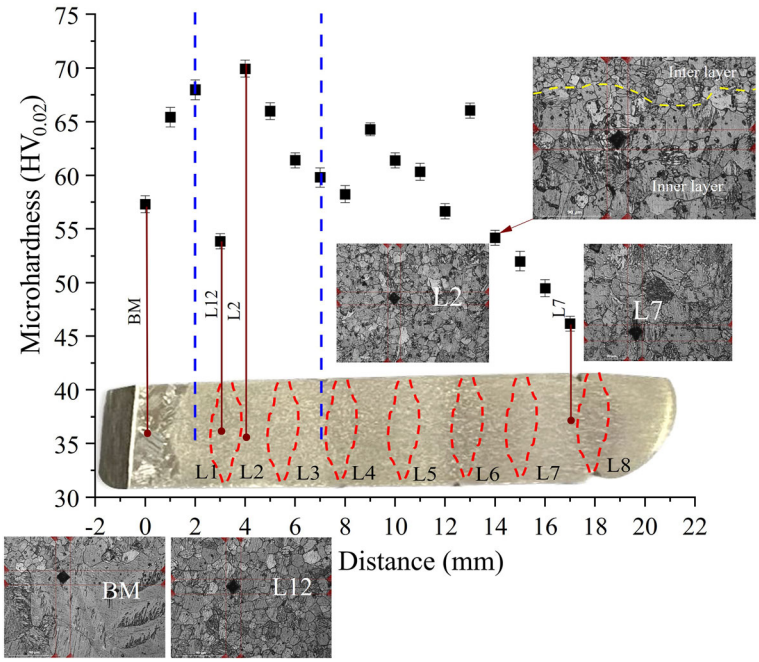

Fig. 10. Microhardness variation of DED-Arc/AZ31.

$HV_{0.02}$, as indicated by point L2 (second layer). The microhardness shows a downward trend as the distance increases from the bottom layer to the top layer owing to the HAE. The microhardness of the top layer was observed to be 46.18 $HV_{0.02}$, which is due to the minor humping defect observed in the top layers. The humping defect is also caused by the HAE which softens the material and causes a hardness reduction. Furthermore, the microhardness of the AM part in the bottom and middle layers is considerably higher than for the base material. This may be due to the increased intensity of

precipitates observed in the DED-Arc/AZ31 sample which strengthens the AM material. The higher microhardness of the BM despite the coarser microstructure may be due to the fact that wrought Mg alloys exhibit better mechanical properties than their counterparts. The sheet metal forming process induces a strain-hardening effect and higher dislocation density which will enhance the hardness of the material.[42]

The mechanical property of the DB interface was analyzed using a microhardness survey, and the microhardness variation across the bond line of the DB sample is shown in Fig. 11. Three readings were taken in parallel lines across the joint with a spacing of 100 μm between the indentations, and the average values are reported. There is no significant variation in microhardness on either side of the bond line. A comparatively higher value of microhardness (65.48 $HV_{0.02}$) is observed at the joint interface due to the DRX in the diffusion reaction zone. This indicates that the bonding process has a considerable effect on the microhardness at the interface.

CONCLUSION

Diffusion bonding (DB) of an additively manufactured (AM) AZ31 Mg alloy has been investigated for the first time. The microstructural and elemental distribution analysis and microhardness survey were carried out on a DB sample with optimized process parameters such as a temperature of 470°C, bonding pressure of 10 MPa, and holding time of 60 min. A monolithic structure was obtained which shows the prospective use of DB as a promising technology for joining/repairing AM components. From the microstructural and microhardness analysis of the DED-Arc AZ31 and DB sample, the following observations were made.

1. A high-integrity DB joint of DED-Arc/AZ31 was achieved in a non-vacuum furnace with special interface treatment. The Ga treatment at the interface prevents the reoxidation of the faying surfaces at the bonding temperature, and hence metallic contact has been established.
2. The uniform elemental distribution at the interface, like the parent metal, emphasizes the enhanced interdiffusion of atoms across the joint line, and the formation of a void-free joint. The elemental mass% at the joint interface was observed as Mg— 96.88%, Al— 2.78%, and Zn— 0.34% from the EPMA qualitative analysis.
3. A high intensity of precipitate phases was observed in the DED-Arc/AZ31 and DB samples. The precipitation of β-$Mg_{17}Al_{12}$ contributes to the precipitation-strengthening of the AZ31 alloy by pinning the grain boundaries and acts as a hindrance to the dislocation movement.
4. Discontinuous dynamic recrystallization characterized by GB bulging and strain-induced GB migration was observed at the joint interface. GBs perpendicular to the interface gradually migrate across the interface to form stable TJs. Grain refinement was observed in the diffusion reaction zone due to the localized plastic deformation. Consequently, higher microhardness was observed in the joint zone.

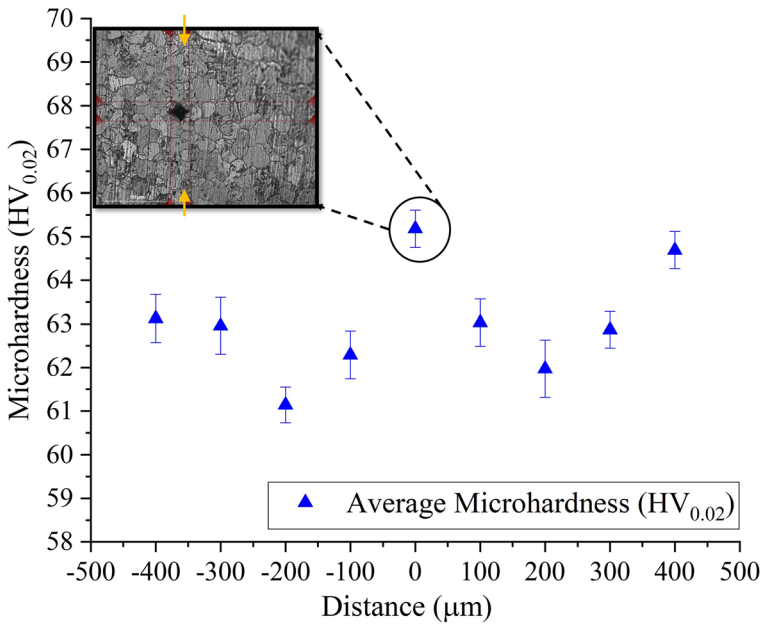

Fig. 11. Microhardness variation of DB joint.

ACKNOWLEDGEMENT

The authors acknowledge the central research facility at IIT Delhi for use of the FESEM TESCAN and EPMA facilities and Prof. Suresh Neelakantan, Department of Materials Science and Engineering, IIT Delhi for providing EBSD facility.

CONFLICT OF INTEREST

The authors declare that they have no known competing financial interests or personal relationships that could have appeared to influence the work reported in this paper.

REFERENCES

1. ASTM 52900, *ASTM Int.* **2021**, 1 (2021).
2. E. Aldalur, A. Suárez, and F. Veiga, *J. Mater. Process. Technol.* **297**, (2021).
3. Y. Guo, G. Quan, Y. Jiang, L. Ren, L. Fan, and H. Pan, *J. Magnes. Alloy.* 9, 192 (2021).
4. X. Duan, Q. Li, W. Xie, and X. Yang, *J. Mater. Process. Technol.* **311**, (2023).
5. P. Wang, H. Zhang, H. Zhu, Q. Li, and M. Feng, *J. Mater. Process. Technol.* 288, 116895 (2021).
6. K. G. Prashanth, R. Damodaram, S. Scudino, Z. Wang, K. Prasad Rao, and J. Eckert, *Mater. Des.* **57**, 632 (2014).
7. K.G. Prashanth, R. Damodaram, T. Maity, P. Wang, and J. Eckert, *Mater. Sci. Eng. A* 704, 66 (2017).
8. J. Wang, Y. Wang, and J. Shi, *Int. J. Adv. Manuf. Technol.* 115, 1037 (2021).
9. R. Dipin Kumar, Y. Koli, and S. Aravindan, *Mater. Lett.* **337**, 133976 (2023).
10. W. Zhong and J.C. Zhao, *Acta Mater.* 201, 191 (2020).
11. M. Li, L. Lu, Y. Fan, M. Ma, T. Zhou, F. Qi, H. Zhang, and Z. Wu, *Mater. Today Commun.* 34, 105467 (2023).
12. B. Mordike and T. Ebert, *Mater. Sci. Eng. A* 302, 37 (2001).
13. H. Takagi, H. Sasahara, T. Abe, H. Sannomiya, S. Nishiyama, S. Ohta, and K. Nakamura, *Addit. Manuf.* 24, 498 (2018).
14. K. V, N. Kumar B, S. Kumar S, and V. M, *Addit. Manuf.* **55**, 102802 (2022).
15. J. Wang, Z. Zhao, P. Bai, R. Zhang, Z. Zhang, L. Wang, W. Du, F. Wang, and Z. Huang, *J. Alloys Compd.* 939, 168665 (2023).
16. X. Yang, J. Liu, Z. Wang, X. Lin, F. Liu, W. Huang, and E. Liang, *Mater. Sci. Eng. A* 774, 138942 (2020).
17. X. Fang, J. Yang, S. Wang, C. Wang, K. Huang, H. Li, and B. Lu, *J. Mater. Process. Technol.* 300, 117430 (2022).
18. Y. Koli, N. Yuvaraj, A. Sivanandam, and Vipin, *Proc. Inst. Mech. Eng. Part C J. Mech. Eng. Sci.* **236**, 984 (2022).
19. C. Zhang, H. Li, and M. Li, *JOM* 71, 1175 (2019).
20. L. Han, J. Wang, Y. Chen, Z. Liu, Y. Huang, D. Liu, L. Luo, C. Liu, Y. Liu, and Z. Wang, *J. Mater. Process. Technol.* 302, 117508 (2022).
21. Z. Yang, X. Zhang, J. Cheng, X. Li, and Y. Shen, *Mater. Today Commun.* 35, 105642 (2023).
22. H. Somekawa, H. Watanabe, T. Mukai, and K. Higashi, *Scr. Mater.* 48, 1249 (2003).
23. O. Torun, A. Karabulut, B. Baksan, and I. Çelikyürek, *Mater. Des.* 29, 2043 (2008).
24. X. Tong, L. Zai, G. You, H. Wu, H. Wen, and S. Long, *Mater. Sci. Eng. A* 767, 138408 (2019).
25. M. Joseph Fernandus, T. Senthilkumar, V. Balasubramanian, and S. Rajakumar, *Mater. Des.* **33**, 31 (2012).
26. M. Jafarian, A. Khodabandeh, and S. Manafi, *Mater. Des.* 65, 160 (2015).
27. T. Yang, S. Geng, D. Zhang, K. Wang, C. Guo, and Y. Zhang, *Weld. World* 541 (2023).
28. H. Shakeri and M.A. Mofid, *Met. Mater. Int.* 27, 4132 (2021).
29. N. Nadermanesh, A. Azizi, and S. Manafi, *Proc. Inst. Mech. Eng. Part B J. Eng. Manuf.* **235**, 2118 (2021).
30. T. Klein, A. Arnoldt, M. Schnall, and S. Gneiger, *JOM* 73, 1126 (2021).
31. X. Niu, G. Li, Z. Zhang, P. Zhou, H. Wang, S. Zhang, and W. Cheng, *Mater. Sci. Eng. A* 743, 207 (2019).
32. J.Y. Zhang, M.Y. Sun, B. Xu, X. Hu, S. Liu, B.J. Xie, and D.Z. Li, *Mater. Sci. Eng. A* 746, 1 (2019).
33. Y. Sun, X. Liu, W. Wang, Y. Yang, and W. Zhang, *J. Alloys Compd.* 957, 170390 (2023).
34. L. Zhang, Z. Zhang, L. Huang, L. Wu, Y. Sun, and S. Guan, *JOM* 75, 2374 (2023).
35. H. Zhang, S. Hu, Z. Wang, and Y. Liang, *Mater. Des.* 86, 894 (2015).
36. A. R. Begg, EP 0123382 A1 (1984).
37. A.A. Shirzadi, G. Saindrenan, and E.R. Wallach, *Mater. Sci. Forum* 396–402, 1579 (2002).
38. A.A. Shirzadi, A. Laik, R. Tewari, J. Orsborn, and G.K. Dey, *Materialia* 4, 115 (2018).
39. H. Shi, Y. Huang, Q. Luo, S. Gavras, R. Willumeit-Römer, and N. Hort, *J. Magnes. Alloy.* 10, 3289 (2022).
40. Z. Zhou, Y. Cui, Q. Wu, G. Xu, L. Zhou, and Y. Cui, *Calphad Comput. Coupling Phase Diagrams Thermochem.* **78**, (2022).
41. A.A. Nayeb-Hashemi and J.B. Clark, *Bull. Alloy Phase Diagrams* 6, 434 (1985).
42. S.W. Lee, S.-H. Kim, and S.H. Park, *J. Magnes. Alloy.* 8, 537 (2020).

Publisher's Note Springer Nature remains neutral with regard to jurisdictional claims in published maps and institutional affiliations.

Springer Nature or its licensor (e.g. a society or other partner) holds exclusive rights to this article under a publishing agreement with the author(s) or other rightsholder(s); author self-archiving of the accepted manuscript version of this article is solely governed by the terms of such publishing agreement and applicable law.